

1
2
3
4
5
6
7
8
9
10
11
12
13
14
15
16
17
18
19
20
21

Distinguishing signal from autofluorescence in cryogenic correlated light and electron microscopy of mammalian cells

Stephen D. Carter^{1†}, Shrawan K. Mageswaran^{1†}, Zachary J. Farino², João I. Mamede³, Catherine M. Oikonomou¹, Thomas J. Hope³, Zachary Freyberg^{2,4*}, Grant J. Jensen^{1,5*}

[†] These authors contributed equally to the work.

* Correspondence Jensen@caltech.edu, freyberg@pitt.edu

¹ Division of Biology, California Institute of Technology, Pasadena, CA 91125, USA; ² Department of Psychiatry, University of Pittsburgh, Pittsburgh, PA 15213, USA; ³ Department of Cell and Molecular Biology, Northwestern University, Chicago, IL 60611, USA; ⁴ Department of Cell Biology, University of Pittsburgh, PA 15213, USA; ⁵ Howard Hughes Medical Institute (HHMI), California Institute of Technology, Pasadena, CA 91125, USA.

22 **Abstract**

23 Cryogenic correlated light and electron microscopy (cryo-CLEM) is a valuable tool for studying
24 biological processes *in situ*. In cryo-CLEM, a target protein of interest is tagged with a fluorophore
25 and the location of the corresponding fluorescent signal is used to identify the structure in low-
26 contrast but feature-rich cryo-EM images. To date, cryo-CLEM studies of mammalian cells have
27 relied on very bright organic dyes or fluorescent protein tags concentrated in virus particles. Here
28 we describe a method to expand the application of cryo-CLEM to cells harboring genetically-
29 encoded fluorescent proteins. We discovered that a variety of mammalian cells exhibit strong
30 punctate autofluorescence when imaged under cryogenic conditions (80K). Compared to
31 fluorescent protein tags, these sources of autofluorescence exhibit a broader spectrum of
32 fluorescence, which we exploited to develop a simple, robust approach to discriminate between
33 the two. We validate this method in INS-1E cells using a mitochondrial marker, and apply it to study
34 the ultrastructural variability of secretory granules in a near-native state within intact INS-1E
35 pancreatic cells by high-resolution 3D electron cryotomography.

36

37

38

39 Introduction

40 Electron microscopy (EM) is an essential tool in the study of cell ultrastructure, with resolving power
41 several orders of magnitude greater than that of light microscopy (LM). Frequently, however, it is
42 difficult to identify objects of interest in EM images when their ultrastructure is unknown. In
43 conventional “thin-section” transmission electron microscopy (TEM), this challenge was addressed
44 by the development of immuno-gold labeling (Faulk and Taylor 1971). Although this method allows
45 direct labeling and visualization of specific targets within the cell, the fixation, dehydration and/or
46 resin embedding steps can result in poor cell and antigen preservation and accompanying loss of
47 information.

48
49 Alternatively, in correlated light and electron microscopy (CLEM), each target can be specifically
50 labelled with a genetically-encoded fluorescent protein (Briegel, Chen et al. 2010), located first by
51 fluorescence light microscopy, and then imaged at higher magnification by electron microscopy.
52 CLEM can be done either at room- or cryogenic-temperatures (“cryo-CLEM”). Like immunoEM,
53 room-temperature CLEM also requires chemically fixed and dehydrated cells, which can distort or
54 obscure important structural features (Afzelius and Maunsbach 2004, Lucic, Rigort et al. 2013), but
55 it has nevertheless allowed the visualization of numerous bacterial and mammalian cellular events
56 that would otherwise have been challenging or impossible to capture (Voloshin Ia, Suslov le et al.
57 2000, Grabenbauer, Geerts et al. 2005, Darcy, Staras et al. 2006, Kapoor, Lampson et al. 2006,
58 Muller-Reichert, Srayko et al. 2007, Kukulski, Schorb et al. 2011, Kukulski, Schorb et al. 2012,
59 Redemann and Muller-Reichert 2013, Avinoam, Schorb et al. 2015, Bertipaglia, Schneider et al.
60 2016, Schorb, Gaechter et al. 2016).

61 In cryo-CLEM samples are preserved in a near-native, “frozen-hydrated” state. To visualize
62 fluorescence inside frozen-hydrated cells, cryogenic LM (cryo-LM) stages are used (Briegel,
63 Chen et al. 2010, Schlimpert, Klein et al. 2012, Schellenberger, Kaufmann et al. 2014, Schorb
64 and Briggs 2014, Bertipaglia, Schneider et al. 2016, Schorb, Gaechter et al. 2016). Unfortunately,
65 because the sample has to be kept frozen, long-working-distance air objective lenses with low
66 numerical apertures are used instead of oil-immersion lenses. To increase the resolution of the
67 light microscopy, several “super-resolution” cryo-CLEM studies have also now been performed
68 (Chang, Chen et al. 2014, Liu, Xue et al. 2015).

69

70 To date, cryo-CLEM studies of mammalian cells have used either very bright organic fluorescent
71 dyes or fluorescent proteins concentrated in viruses (Jun, Ke et al. 2011, Schellenberger,
72 Kaufmann et al. 2014, Bykov, Cortese et al. 2016). Organic dyes are very bright, but it can be
73 challenging to attach them to specific proteins inside cells. Genetically-encoded fluorescent
74 proteins, on the other hand, can be easily fused with most proteins and offer a richer repertoire of
75 colors, but they are much less bright, so their signals can be more difficult to distinguish from
76 cellular autofluorescence. Here we describe a method to distinguish signal arising from
77 genetically-encoded fluorescent proteins from endogenous autofluorescence in mammalian cells
78 under cryogenic conditions. We validate the approach with mitochondria and then demonstrate
79 how the method allows secretory granules to be identified and structurally characterized within
80 intact pancreatic cells with unprecedented resolution.

81

82

83

84

85 **Results**

86 **INS-1E cells exhibit bright, punctate autofluorescence at ~80K**

87 Initially, we set out to image the secretory pathway of the pancreatic beta cell-derived INS-1E line,
88 which has long been used as a model system (Merglen, Theander et al. 2004, Farino, Morgenstern
89 et al. 2016). The secretory machinery of these cells has been well studied by both LM and
90 conventional EM (Rubi, Ljubicic et al. 2005, Giordano, Brigatti et al. 2008), but we wanted to
91 advance that by imaging cells in a near-native, frozen-hydrated state in 3-D by using electron
92 cryotomography (ECT) (Oikonomou and Jensen 2016). We were particularly interested in dense
93 core secretory granules (DCSGs), which are central to the efficient secretion of hormones including
94 insulin (Kim, Tao-Cheng et al. 2001). To identify DCSGs in cryotomograms, we tagged
95 chromogranin A (CgA), a granin protein widely used as a marker for DCSGs given its almost
96 exclusive localization to this intracellular compartment (Huh, Bahk et al. 2005).

97

98 We transfected INS-1E cells with CgA C-terminally tagged with GFP and grew cells to around 30-
99 40% confluency on EM finder grids. To facilitate image correlation we added 500 nm blue
100 fluorospheres visible in both cryo-LM and cryo-EM modalities to the samples before plunge-
101 freezing [as in (Chang, Chen et al. 2014, Schellenberger, Kaufmann et al. 2014, Schorb and Briggs
102 2014, Liu, Xue et al. 2015, Bykov, Cortese et al. 2016)]. We first performed cryo-LM to identify
103 targets of interest in thin ice at the periphery of cells. To accommodate the relatively dim signal of
104 CgA-GFP (due either to the low temperature or the low NA of our long working-distance air
105 objective (NA 0.7), or both), we used exposure times of up to 2 seconds and applied a 2D real-

106 time deconvolution algorithm. We observed a punctate cytosolic distribution (Figure 1A) consistent
107 with CgA's expected intracellular localization to secretory granules (Huh, Bahk et al. 2005).

108

109 As a negative control, we also imaged untransfected INS-1E cells by cryo-LM (Figure 1b). Unlike
110 room-temperature images of untransfected cells, which display little autofluorescence (Figure 1c-
111 d), to our surprise unlabelled INS-1E cells exhibited clear puncta at ~80K (cooled by liquid
112 nitrogen). To determine whether the autofluorescence observed at 80K was broad-spectrum, as is
113 typical at room-temperature (Billinton and Knight 2001), we also imaged untransfected and
114 transfected cells using an mCherry filter. In transfected cells there were two populations of puncta:
115 one emitting both green and red fluorescence, and one emitting primarily green fluorescence
116 (Figure 1a). In untransfected cells, all the puncta emitted both green and red fluorescence (Figure
117 1b), indicating that the autofluorescence in the sample was broad spectrum.

118

119 **Other mammalian cells also exhibit bright autofluorescence at ~80K**

120 Next we checked if bright autofluorescence at 80K was unique to INS-1E cells. We applied the
121 same imaging technique to three other untransfected cell lines: rhesus macaque fibroblasts, HeLa
122 cells and human primary adipocytes. All three cell lines exhibited numerous puncta distributed
123 throughout the cell volume with broad fluorescence spectra ranging from green (FITC) to red
124 (mCherry) (Figure 2). To identify the source of the observed autofluorescence, we imaged several
125 puncta at high-resolution by ECT. All of the autofluorescent puncta in rhesus macaque fibroblasts
126 (Figure 3a) and HeLa cells (data not shown) correlated to multimembranous structures, some
127 resembling multilamellar bodies (MLBs) (Hariri, Millane et al. 2000, Lajoie, Guay et al. 2005).
128 Similarly, many autofluorescent puncta in untransfected INS-1E cells also correlated to

129 multimembranous structures in cryotomograms (Figure 3b, panel 1-3). Other autofluorescent
130 puncta in INS-1E cells correlated to membrane-enclosed crystals (Figure 3b, panel 4).

131

132 **Distinguishing fluorescent protein tags from autofluorescence**

133 At room temperature, the confounding effect of cellular autofluorescence can sometimes be
134 mitigated by photobleaching; background fluorescence sources tend to bleach faster than
135 fluorescent proteins (Billinton and Knight 2001). Unfortunately, the autofluorescence we observed
136 at 80K did not bleach away quickly (data not shown), as observed previously for exogenous
137 fluorophores (Schwartz, Sarbash et al. 2007). Instead, we tried to identify autofluorescence by its
138 broader emission spectrum, as has been done previously at room temperature (Szollosi, Lockett
139 et al. 1995, Mansfield, Gossage et al. 2005).

140

141 To test the method, we chose a “positive control” that could be unambiguously identified in
142 cryotomograms with or without a fluorescent tag. Mitochondria proved to be a good choice due to
143 their well-defined ultrastructure including easily-recognizable cristae (Rabl, Soubannier et al. 2009,
144 Zick, Rabl et al. 2009, Davies, Daum et al. 2014). We transfected INS-1E cells with the
145 mitochondrial marker Mito-DsRed2, which is targeted to the space between the inner and outer
146 mitochondrial membrane by the signal sequence of cytochrome C oxidase. We again imaged both
147 untransfected and transfected cells by cryo-CLEM, and measured the fluorescence of a large
148 number of puncta in both the green (FITC) and red (mCherry) channels. While both samples
149 exhibited puncta emitting in both the mCherry and FITC channels, there was a population only in
150 the transfected cells that exhibited high intensity in the mCherry channel and low intensity in the
151 FITC channel (Figure 4a, top left corner), indicative of specific Mito-DsRed2 fluorescence.

152 To identify structures associated with fluorescence in these cells, we imaged 32 randomly chosen
153 puncta in transfected cells by ECT. Many of the puncta correlated to mitochondria, and the centroid
154 of fluorescence fell within the boundaries of the organelle, validating the accuracy of our correlation
155 procedure (Figure 4b, targets 1-7). Others correlated to multimembranous structures (Figure 4b,
156 targets 8-11). As expected, puncta correlating to mitochondria exhibited a greater ratio of red
157 fluorescence to green fluorescence, and were therefore positioned near the upper left corner of the
158 fluorescence plot (Figure 4a). The multimembranous structures corresponded to puncta near the
159 opposite (lower right) corner. Thus, to distinguish fluorescent protein tags from autofluorescence,
160 one can record fluorescence images of both tagged and untagged frozen cells and plot the
161 fluorescence in two channels. Puncta in the overlap region near the middle of the plot may be from
162 either fluorescent protein tags or autofluorescence, and cannot be distinguished with great
163 confidence. Puncta in the extreme corner towards the pure color of the fluorescent protein tag
164 where autofluorescent puncta are not seen (triangle in the upper left corner of Figure 4a), however,
165 are very likely to contain the tag.

166

167 **Cryo-CLEM of INS-1E cells transfected with chromogranin A-GFP**

168 Having established a technique to distinguish signal from autofluorescence, we returned to INS-
169 1E cells expressing CgA-GFP. Once again, we imaged both untransfected and transfected cells
170 by cryo-LM, recorded their intensity values in the green (FITC) and red (mCherry) channels, and
171 plotted these values in two dimensions (Figure 5a). As expected, we observed a broad overlap
172 region in the center of the plot with puncta from both the transfected (tagged) and untransfected
173 (untagged) cells. We also observed a region in the upper left corner of the plot devoid of puncta
174 from untransfected cells which very likely contained CgA-GFP-specific signal.

175

176 Twenty-seven puncta were then imaged by ECT, including 15 in the upper left corner of the plot
177 and 12 in the ambiguous overlap region. Cryotomographic slices through ten examples are shown
178 in Figure 5b (see also Supplementary Movie 1). Among the puncta from the upper left corner of
179 the plot (very likely to contain CgA-GFP), we observed vesicles with a dense aggregate core (#'s
180 4 and 6 for example), vesicles with a dense granular core (#5 for example), vesicles with a dense
181 aggregate or granular core and internal smaller vesicles (#'s 1 and 3 for example), and clusters of
182 dense aggregated material partially surrounded by membrane fragments (#'s 2 and 7). Among the
183 puncta in the ambiguous overlap region we saw two vesicles with crystalline cores (#'s 8 and 10)
184 and a cluster of very dense aggregated material (# 9).

185

186 **Discussion**

187 Here we report the discovery that many mammalian cell lines exhibit strong punctate
188 autofluorescence at ~80K and an approach to distinguish fluorescent protein tags from this
189 autofluorescence.

190

191 Cellular autofluorescence at room temperature is known to arise from multiple sources including
192 (1) biomolecules such as amino acids containing aromatic rings, (2) the three-ring system of flavins
193 (producing green spectra) (Benson, Meyer et al. 1979, Jackson, Snyder et al. 2004), (3) the
194 reduced form of pyridine nucleotides (NAD(P)H, producing blue/green spectra) (Chance and
195 Thorell 1959, Galeotti, Van Rossum et al. 1970), (4) lipid pigments (orange/yellow spectra) (Dayan
196 and Wolman 1993, Billinton and Knight 2001), (5) porphyrins (red spectra), and (6) chlorophyll
197 (Sheen, Hwang et al. 1995). Various strategies have been developed to overcome

198 autofluorescence at room temperature including bleaching it away (Viegas, Martins et al. 2007,
199 Kumar, Sandhyamani et al. 2015), quenching it with additives (Cowen, Haven et al. 1985, Schnell,
200 Staines et al. 1999, Billinton and Knight 2001, Kumar, Sandhyamani et al. 2015), or detecting its
201 spectral signature (Steinkamp and Stewart 1986, Van de Lest, Versteeg et al. 1995, Neumann and
202 Gabel 2002, Dickinson, Simbuerger et al. 2003, Gareau, Bargo et al. 2004, Mansfield, Gossage et
203 al. 2005).

204

205 Here we found that at ~80K, autofluorescence is produced by multimembranous structures and
206 what in cell line INS-1E were most likely insulin crystals. The multimembranous structures, which
207 in some cases exhibited up to 14 tightly nested concentric spherical vesicles, resembled MLBs
208 (Hariri, Millane et al. 2000, Lajoie, Guay et al. 2005). Others, bounded by a single outer membrane
209 and containing what looked like partially degraded membranes and other materials are most likely
210 autolysosomes (Klionsky, Eskelinen et al. 2014, Klumperman and Raposo 2014). Earlier work by
211 König et al. also provided evidence that intracellular autofluorescence was more pronounced at
212 80K than at room temperature, and attributed this to the increase in quantum yield of the
213 fluorophores due to the reduction in thermal relaxation processes at lower temperatures (Konig,
214 Uchugonova et al. 2014).

215

216 Since the excitation and emission peaks of autofluorescence overlap with those of commonly used
217 fluorophores such as GFP, YFP and mCherry, filter cubes will not adequately discriminate
218 autofluorescence from signal at 80K. Instead, we recommend first characterizing the
219 autofluorescence by recording images of wild-type (untransfected/unlabelled) cells in two
220 channels, one corresponding to the color of a fluorescent protein tag of interest and the other

221 broadly separated, and then plotting the fluorescence intensities in the two channels in a two-
222 dimensional plot. Next, we recommend imaging a random subset of these puncta by ECT to
223 determine the structures of the sources of autofluorescence in the cell type being studied. Cells
224 labelled with the fluorescent protein tag should then be imaged by cryo-LM in both channels and
225 their fluorescence intensities plotted as before. Puncta exhibiting strong fluorescence in the
226 channel of interest and lying outside the scatter plot region containing puncta from unlabelled cells
227 are very likely to contain the fluorescent protein tag, and not be due simply to autofluorescence.
228 This method requires no specialized equipment and is compatible with a standard cryo-CLEM
229 workflow.

230

231 **Cryo-CLEM/ECT of the secretory pathway of INS-1E cells**

232 To demonstrate the utility of the method, we used cryo-CLEM to identify objects containing CgA
233 inside pancreatic cells. These secretory cells are characterized by the ability to rapidly release
234 large amounts of proteins through specialized trans-Golgi network (TGN)-derived vesicles which
235 by traditional EM of stained, plastic-embedded sections display dense granular cores (Kelly 1985,
236 Burgess and Kelly 1987). The dense nature of these cores is known to derive from chromogranins
237 and secretogranins which aggregate in the TGN as their environment acidifies and becomes
238 calcium-rich prior to vesicle formation, and is also related to increased zinc concentrations which
239 are thought to induce insulin crystallization (Gerdes, Rosa et al. 1989, Gorr, Shioi et al. 1989,
240 Chanat and Huttner 1991, Yoo and Albanesi 1991, Videen, Mezger et al. 1992, Taupenot, Harper
241 et al. 2005, Lemaire, Ravier et al. 2009). Aggregation of granin proteins is thought to facilitate cargo
242 sorting (Burgess and Kelly 1987, Carnell and Moore 1994, Taupenot, Harper et al. 2003).

243

244 Using our method to identify structures that contained CgA-GFP, we observed not just one class
245 of DCSGs, but a diversity of objects including vesicles with a dense aggregate core, vesicles with
246 a granular core, vesicles with a dense aggregate or granular core and internal smaller vesicles,
247 clusters of dense aggregated material partially surrounded by membrane fragments, and a cluster
248 of very dense aggregated material in the cytoplasm with no membrane fragments in the vicinity.
249 We speculate that the first two classes represent different steps in the secretory pathway, and that
250 the last two classes are the result of vesicle lysis. The vesicles with smaller vesicles inside may be
251 autophagosomes, which are known to degrade insulin as a mechanism to regulate secretory
252 function, though they were not clearly surrounded by two membranes as expected for
253 autophagosomes (Marsh, Soden et al. 2007, Goginashvili, Zhang et al. 2015, Liu, Xue et al. 2015).
254 Compared to the conclusions one might have made based on fluorescence microscopy alone (that
255 all puncta represented DCSGs), cryo-CLEM revealed that some of the puncta were lysed vesicles
256 and probable autophagosomes, which may have formed here simply because of the unnatural
257 levels of CgA expression. Moreover, we also observed vesicles by ECT with dense aggregated
258 cores that were not fluorescent (example denoted by α in Figure 5b; see also Supplementary Movie
259 1). One possible explanation for this is that the variable pH within DCSGs effects the fluorescence
260 of GFP. Indeed in insulin containing beta cells, granule acidification is a critical step for proper
261 maturation of pro-insulin to the mature form, ultimately leading to crystallization and exocytosis
262 (Orci, Ravazzola et al. 1986, Paroutis, Touret et al. 2004). Again this highlights a caveat to
263 interpreting fluorescence images: some cellular objects of a given type may not fluoresce or even
264 incorporate tagged protein if it is expressed unnaturally. Finally, our images reveal that some
265 vesicles are largely filled by crystals. Because their lattice spacings matched those of insulin
266 crystals, this suggests that insulin can occupy a remarkably large proportion of the vesicle. In any

267 case our cryo-CLEM/ECT data make it clear that the structures of DCSGs are not uniform, but
268 remarkably diverse, and that further characterization is in order.

269

270 **Online Methods**

271 **Cell growth and transfection**

272 Rat insulinoma INS-1E (gift of P. Maechler, Université de Genève) and human neuroblastoma
273 BE(2)-M17 cells (CRL-2267; American Type Culture Collection, Manassas, VA) were maintained
274 in a humidified 37°C incubator with 5% CO₂. INS-1E cells were cultured in RPMI 1640 media with
275 L-glutamine (Life Technologies, Grand Island, NY), supplemented with 5% fetal bovine serum (heat
276 inactivated), 10 mM HEPES, 100 units/mL penicillin, 100 µg/mL streptomycin, 1 mM sodium
277 pyruvate, and 50 µM 2-Mercapto-ethanol. HeLa cells, rhesus macaque fibroblast and primary
278 adipocyte cells were cultured under similar conditions. For cryo-EM and cryo-ET, cells were plated
279 onto fibronectin-coated 200 mesh gold R2/2 London finder Quantifoil grids (Quantifoil Micro Tools
280 GmbH, Jena, Germany) at a density of 2×10^5 cells/mL. After 48 h incubation, cultures were pre-
281 treated (30 min, 37°C, 5% CO₂) in Krebs Ringers Bicarbonate HEPES buffer (KRBH: 132.2 mM
282 NaCl, 3.6 mM KCl, 5 mM NaHCO₃, 0.5 mM NaH₂PO₄, 0.5 mM MgCl₂, 1.5 mM CaCl₂, and 10 mM
283 HEPES, and 0.1% bovine serum albumin, pH 7.4) supplemented with 2.8 mM glucose before being
284 plunge frozen in liquid ethane/propane mixture using a Vitrobot Mark IV (FEI, Hillsboro, OR) (Iancu,
285 Tivol et al. 2006).. For cell transfections, as above INS-1E cells were plated onto fibronectin-coated
286 200 mesh gold R2/2 Quantifoil grids at a 2×10^5 cells/mL density and cultured for 24-48 h (37°C,
287 5% CO₂). The cells were then transfected with 2 µg DNA constructs in serum-free RPMI media (5
288 h, 37°C, 5% CO₂) using Lipofectamine 2000 (Life Technologies, Carlsbad, CA). Following 16 h
289 incubation in serum-containing RPMI media, cells were washed in KRBH and plunge-frozen for

290 subsequent imaging. Immediately prior to plunge-freezing, 3 μ l of a suspension of beads was
291 applied to grids. The bead suspension was made by diluting 500 nm blue (345/435 nm) polystyrene
292 fluorospheres (Phosphorex) with a colloidal solution of 20 nm gold fiducials (Sigma Aldrich)
293 pretreated with bovine serum albumin. The gold served as fiducial markers for tomogram
294 reconstruction while the blue fluorospheres served as landmarks for registering fluorescence light
295 microscopy (FLM) images from different channels as well as EM images. In addition, the blue
296 fluorospheres helped locate target areas in phase contrast light microscopy and low-magnification
297 EM images containing thin ice suitable for high-resolution ECT. Plunge-frozen grids were
298 subsequently loaded into Polara EM cartridges (FEI). EM cartridges containing frozen grids were
299 stored in liquid nitrogen and maintained at $\leq -150^{\circ}\text{C}$ throughout the experiment including cryo-FLM
300 imaging, cryo-EM imaging, storage and transfer.

301

302 **Fluorescence imaging and Image processing**

303 The EM cartridges were transferred into a cryo-FLM stage (FEI Cryostage) modified to hold Polara
304 EM cartridges (Nickell, Kofler et al. 2006, Briegel, Chen et al. 2010) and mounted on a Nikon Ti
305 inverted microscope. The grids were imaged using a 60 X extra-long working distance air objective
306 (Nikon CFI S Plan Fluor ELWD 60x NA 0.7 WD 2.62-1.8 mm). Images were recorded using a Neo
307 5.5 sCMOS camera (Andor Technology, South Windsor, CT) using a real-time deconvolution
308 module in the NIS Elements software (Nikon Instruments Inc., Melville, NY). The pixel size
309 corresponding to the objective lens was ~ 108 nm (at the sample level). All fluorescence images
310 (individual channels) were saved in 16-bit grayscale format. CgA-GFP was visualized with a FITC
311 filter. Mito-dsRed2 was visualized with an mCherry filter. Blue fluorospheres were visualized with
312 a DAPI filter. Following FLM imaging, images from different channels were aligned (as described

313 above) using either a module in the NIS Elements software or a Python alignment script written in-
314 house. The 500 nm blue fluorospheres were used to align the DAPI, FITC and YFP channels while
315 autofluorescent puncta were used to align the mCherry channel with the others. The fluorescence
316 channels were aligned to subpixel accuracy. Before the FLM images were further analyzed,
317 background fluorescence in each channel was subtracted from the respective images. This
318 background fluorescence was uniform throughout each image (even outside cellular areas) and
319 likely originates from the grid/ice. Fluorescent puncta were identified in the channel of interest using
320 an in-house python script and their peak fluorescence intensities measured. In addition, intensities
321 of the same pixels in other channels were also recorded. For example, in the case of CgA-GFP
322 dataset, peak intensities of puncta in the FITC channel and their corresponding pixel intensities in
323 the mCherry channel were recorded. Peak intensity values in both channels of both untransfected
324 and transfected cells were plotted on scatter plots.

325

326 **Cryo-CLEM and ECT**

327 Grids previously imaged by FLM were subsequently imaged by ECT using an FEI G2 Polara 300kV
328 FEG TEM equipped with an energy filter (slit width 20 eV for higher magnifications; Gatan, Inc.).
329 Images were recorded using a 4k x 4k K2 Summit direct detector (Gatan, Inc.) operating in the
330 electron counting mode. First, areas containing the fluorescent puncta of interest were located in
331 the TEM. Tilt series were then recorded of these areas using UCSF Tomography (Zheng,
332 Keszthelyi et al. 2007) or SerialEM (Mastronarde 2005) software at a magnification of 18,000X.
333 This corresponds to a pixel size of 6 Å (at the specimen level) and was found to be sufficient for
334 this study. Each tilt series was collected from -60° to +60° with an increment of 1° in an automated

335 fashion at 8-10 μm underfocus. The cumulative dose of one tilt-series was between 80 and 200 e^-
336 $/\text{\AA}^2$.

337

338 Areas of interest were located by TEM in a stepwise manner. First, the grid square/cell of interest
339 on the finder grid was located by using large location markers or other features visible at a low
340 magnification (100 X). Second, a smaller area containing the fluorescent punctum of interest was
341 located by mapping FLM images to intermediate-magnification EM images (typically 3,000X or
342 1,200X) by eye using various local features within the identified grid square. These features
343 included (1) clusters of 500 nm microspheres that were arranged in a uniquely identifiable pattern,
344 (2) cracks and regularly spaced 2 μm holes in the carbon film and (3) ice contamination. This was
345 done with either UCSF Tomography (Zheng, Keszthelyi et al. 2007) or SerialEM (Mastronarde
346 2005) . With UCSF Tomography, the area of interest first had to be mentally mapped on the
347 low/intermediate magnification EM image using the local features described above before being
348 identified again at 18,000 X magnification by the same features (if available within the field of view).
349 Correlation with SerialEM was more streamlined. FLM images were registered with EM images of
350 the grid square of interest using local features (described above) as control points. These EM
351 images could be either single projection images at a low enough magnification (360X or 1,200X)
352 to contain the area of interest and enough control points to enable tilt-series collection or a montage
353 assembled from higher-magnification (3,000X) EM images. Once the FLM images were registered,
354 areas of interest were marked using the “anchor maps” feature. Using this feature, marked areas
355 could be revisited and tilt-series collected in an automated fashion. Once acquired, tilt-series were
356 aligned and binned four-fold into 1k x 1k arrays before reconstruction into 3D tomograms with the
357 IMOD software package (Kremer, Mastronarde et al. 1996). In addition to the tilt-series, projection

358 images of the location at various magnifications (360X, 1,200X, 3,000X, 9,300X and 18,000X) were
359 saved and used for high-precision post-data collection correlation.

360

361 **High-precision post-data collection correlation of FLM images and tomographic slices**

362 RGM fluorescence images were correlated to EM projection images using an in-house image
363 registration script written in Python. This entailed stepwise registration of images recorded at
364 various magnifications, starting with the FLM image, recorded at the lowest magnification (60X),
365 all the way up to the 18,000X EM image. First, the FLM image was registered with a
366 low/intermediate-magnification EM image. The centroid positions of 500 nm blue microspheres
367 were estimated to sub-pixel accuracy and used as control points for this registration. The
368 magnification of the EM image used for this registration was chosen such that there were at least
369 4 control points available in the field of view. The microspheres were clearly visible at
370 magnifications above 1,200X and less reliably visible at magnifications as low as 360X. Therefore
371 the registration process was more accurate when using >1,200X EM images. The registration
372 parameters (affine transformation) were saved. Successive steps involved similar calculation of
373 affine transformation parameters between EM projection images of various magnifications up to
374 18,000X. Gold fiducials, surface ice contaminations, and cellular features visible at these
375 magnifications were used as control points for these registration steps. In general, we found that
376 high defocus values at lower magnifications (~50 μm at 3,000X and ~1 mm at 1,200X) enhanced
377 the visibility of control points and thus resulted in better registration. Also, having more control
378 points (at least 5) resulted in better registration. Precise registration at lower magnifications is
379 particularly important because of the relatively larger pixel sizes involved. To produce the final
380 registration of the FLM images with the 18,000X projection EM images, the transformations

381 calculated in each of the previous steps were successively applied to the FLM images. The
382 resulting FLM images were overlaid on the 18,000X EM projection images using Adobe Photoshop
383 CC (San Jose, CA), setting the visibility of the upper FLM image layer to linear dodge.

384

385 **Acknowledgments**

386 This work was supported by the NIH (grant GM082545 to G.J.J., grant GM082545-6935 to T.J.H.,
387 grant K08 DA031241 to Z.F, the Department of Defense (grant PR141292 to Z.F.), and the John
388 F. and Nancy A. Emmerling Fund of The Pittsburgh Foundation (to Z.F.). We thank Dr. Joachim
389 Frank, Dr. Maïté Courel, Dr. Hans Breunig, Robert Grassucci and Stephanie Siegmund for
390 guidance, suggestions and reagents. We thank Dr. Pierre Maechler for generously providing INS-
391 1E cells for our studies.

392

393

394

395

396

397

398

399

400

401

402

403

404 **Figure Legends**

405 **Figure 1. INS-1E cells exhibit strong autofluorescence at 80K. (a,b)** Cryo-LM images
406 (composite of bright field and epifluorescence in FITC, mCherry and DAPI channels) of INS-1E
407 cells transfected with CgA-GFP (A) or untransfected (B). **(c,d)** Room-temperature light microscopy
408 images of epifluorescence in FITC channel of INS-1E cells transfected with CgA-GFP (C) or
409 untransfected (D).

410

411 **Figure 2. Autofluorescence at 80K is a general feature of mammalian cells.** Cryo-LM images
412 (bright field and epifluorescence in FITC, mCherry and DAPI channels) of **(a)** rhesus macaque
413 fibroblasts, **(b)** HeLa cells and **(c)** primary adipocytes.

414

415 **Figure 3. Cryo-CLEM reveals sources of autofluorescence in untransfected rhesus macaque**
416 **fibroblasts (a) and INS-1E cells (b).** Left panels show epifluorescence images overlaid on high-
417 magnification cryo-EM projection images. Middle panel in (b) shows the corresponding
418 tomographic slice. Right panels show zoomed-in views of the boxed areas in corresponding panels
419 at left. Numbers indicate corresponding locations. Scale bars = 200 nm.

420

421 **Figure 4. Relative fluorescence intensity can distinguish target fluorescent signal from**
422 **autofluorescence at 80K. (a)** Scatter plot of mCherry and FITC channel intensity values of
423 fluorescent puncta in INS-1E cells untransfected (magenta) or transfected with Mito-DsRed2
424 (blue). [n > X00 for transfected, X00 untransfected.] The black line indicates the area of the scatter
425 plot with no puncta in untransfected INS-1E cells and is described in the text. Larger symbols
426 denote structures observed by cryo-CLEM of selected puncta in transfected cells, corresponding

427 to mitochondria (triangles) or multi-membraned structures, dense vesicles, crystalline structures or
428 structures with a combination of these features (circles). **(b)** Examples of structures correlated to
429 fluorescent puncta. Left panels show epi-fluorescence images overlaid on high-magnification cryo-
430 EM projection images. Middle panels show tomographic slices of the same areas. Right panels
431 show zoomed-in views of the boxed areas in the middle panels. Numbers indicate corresponding
432 locations. Scale bars = 200 nm.

433

434 **Figure 5. Application of method enables cryo-CLEM of CgA-GFP in INS-1E cells. (a)** Scatter
435 plot of FITC and mCherry channel intensity values of fluorescent puncta in INS-1E cells
436 untransfected (magenta) or transfected with CgA-GFP (blue). [n > X00 for transfected, X00
437 untransfected.] The black line indicates the area of the scatter plot with no puncta in untransfected
438 INS-1E cells and is described in the text. Larger symbols denote structures observed by cryo-
439 CLEM of selected puncta in transfected cells (circles). **(b)** Examples of structures correlated to
440 fluorescent puncta. Left panels show epi-fluorescence images overlaid on high-magnification cryo-
441 EM projection images. Middle panels show tomographic slices of the same areas. Right panels
442 show zoomed-in views of the boxed areas in the middle panels. Numbers indicate corresponding
443 locations. Scale bars = 200 nm.

444

445

446

447

448

449

450 References

- 451 Afzelius, B. A. and A. B. Maunsbach (2004). "Biological ultrastructure research; the first 50
452 years." *Tissue Cell* **36**(2): 83-94.
- 453 Avinoam, O., M. Schorb, C. J. Beese, J. A. Briggs and M. Kaksonen (2015). "ENDOCYTOSIS.
454 Endocytic sites mature by continuous bending and remodeling of the clathrin coat." *Science*
455 **348**(6241): 1369-1372.
- 456 Benson, R. C., R. A. Meyer, M. E. Zaruba and G. M. McKhann (1979). "Cellular
457 autofluorescence--is it due to flavins?" *J Histochem Cytochem* **27**(1): 44-48.
- 458 Bertipaglia, C., S. Schneider, A. J. Jakobi, A. K. Tarafder, Y. S. Bykov, A. Picco, W. Kukulski, J.
459 Kosinski, W. J. Hagen, A. C. Ravichandran, M. Wilmanns, M. Kaksonen, J. A. Briggs and C.
460 Sachse (2016). "Higher-order assemblies of oligomeric cargo receptor complexes form the
461 membrane scaffold of the Cvt vesicle." *EMBO Rep* **17**(7): 1044-1060.
- 462 Billinton, N. and A. W. Knight (2001). "Seeing the wood through the trees: a review of techniques
463 for distinguishing green fluorescent protein from endogenous autofluorescence." *Anal Biochem*
464 **291**(2): 175-197.
- 465 Briegel, A., S. Chen, A. J. Koster, J. M. Plitzko, C. L. Schwartz and G. J. Jensen (2010).
466 "Correlated light and electron cryo-microscopy." *Methods Enzymol* **481**: 317-341.
- 467 Burgess, T. L. and R. B. Kelly (1987). "Constitutive and regulated secretion of proteins." *Annu*
468 *Rev Cell Biol* **3**: 243-293.
- 469 Bykov, Y. S., M. Cortese, J. A. Briggs and R. Bartenschlager (2016). "Correlative light and
470 electron microscopy methods for the study of virus-cell interactions." *FEBS Lett* **590**(13): 1877-
471 1895.
- 472 Carnell, L. and H. P. Moore (1994). "Transport via the regulated secretory pathway in semi-intact
473 PC12 cells: role of intra-cisternal calcium and pH in the transport and sorting of secretogranin II."
474 *J Cell Biol* **127**(3): 693-705.
- 475 Chanat, E. and W. B. Huttner (1991). "Milieu-induced, selective aggregation of regulated
476 secretory proteins in the trans-Golgi network." *J Cell Biol* **115**(6): 1505-1519.
- 477 Chance, B. and B. Thorell (1959). "Localization and kinetics of reduced pyridine nucleotide in
478 living cells by microfluorometry." *J Biol Chem* **234**: 3044-3050.
- 479 Chang, Y. W., S. Chen, E. I. Tocheva, A. Treuner-Lange, S. Lobach, L. Sogaard-Andersen and
480 G. J. Jensen (2014). "Correlated cryogenic photoactivated localization microscopy and cryo-
481 electron tomography." *Nat Methods* **11**(7): 737-739.
- 482 Cowen, T., A. J. Haven and G. Burnstock (1985). "Pontamine sky blue: a counterstain for
483 background autofluorescence in fluorescence and immunofluorescence histochemistry."
484 *Histochemistry* **82**(3): 205-208.
- 485 Darcy, K. J., K. Staras, L. M. Collinson and Y. Goda (2006). "An ultrastructural readout of
486 fluorescence recovery after photobleaching using correlative light and electron microscopy." *Nat*
487 *Protoc* **1**(2): 988-994.
- 488 Davies, K. M., B. Daum, V. A. Gold, A. W. Muhleip, T. Brandt, T. B. Blum, D. J. Mills and W.
489 Kuhlbrandt (2014). "Visualization of ATP synthase dimers in mitochondria by electron cryo-
490 tomography." *J Vis Exp*(91): 51228.
- 491 Dayan, D. and M. Wolman (1993). "Lipid pigments." *Prog Histochem Cytochem* **25**(4): 1-74.
- 492 Dickinson, M. E., E. Simbuerger, B. Zimmermann, C. W. Waters and S. E. Fraser (2003).
493 "Multiphoton excitation spectra in biological samples." *J Biomed Opt* **8**(3): 329-338.

494 Farino, Z. J., T. J. Morgenstern, J. Vallaghe, N. Gregor, P. Donthamsetti, P. E. Harris, N. Pierre,
495 R. Freyberg, F. Charrier-Savournin, J. A. Javitch and Z. Freyberg (2016). "Development of a
496 Rapid Insulin Assay by Homogenous Time-Resolved Fluorescence." *PLoS One* **11**(2): e0148684.
497 Faulk, W. P. and G. M. Taylor (1971). "An immunocolloid method for the electron microscope."
498 *Immunochemistry* **8**(11): 1081-1083.
499 Galeotti, T., G. D. Van Rossum, D. Mayer and B. Chance (1970). "Fluorescence studies of
500 NAD(P)H binding in intact cells." *Hoppe Seylers Z Physiol Chem* **351**(3): 274-275.
501 Gareau, D. S., P. R. Bargo, W. A. Horton and S. L. Jacques (2004). "Confocal fluorescence
502 spectroscopy of subcutaneous cartilage expressing green fluorescent protein versus cutaneous
503 collagen autofluorescence." *J Biomed Opt* **9**(2): 254-258.
504 Gerdes, H. H., P. Rosa, E. Phillips, P. A. Baeuerle, R. Frank, P. Argos and W. B. Huttner (1989).
505 "The primary structure of human secretogranin II, a widespread tyrosine-sulfated secretory
506 granule protein that exhibits low pH- and calcium-induced aggregation." *J Biol Chem* **264**(20):
507 12009-12015.
508 Giordano, T., C. Brigatti, P. Podini, E. Bonifacio, J. Meldolesi and M. L. Malosio (2008). "Beta cell
509 chromogranin B is partially segregated in distinct granules and can be released separately from
510 insulin in response to stimulation." *Diabetologia* **51**(6): 997-1007.
511 Goginashvili, A., Z. Zhang, E. Erbs, C. Spiegelhalter, P. Kessler, M. Mihlan, A. Pasquier, K.
512 Krupina, N. Schieber, L. Cinque, J. Morvan, I. Sumara, Y. Schwab, C. Settembre and R. Ricci
513 (2015). "Insulin granules. Insulin secretory granules control autophagy in pancreatic beta cells."
514 *Science* **347**(6224): 878-882.
515 Gorr, S. U., J. Shioi and D. V. Cohn (1989). "Interaction of calcium with porcine adrenal
516 chromogranin A (secretory protein-I) and chromogranin B (secretogranin I)." *Am J Physiol* **257**(2
517 Pt 1): E247-254.
518 Grabenbauer, M., W. J. Geerts, J. Fernandez-Rodriguez, A. Hoenger, A. J. Koster and T. Nilsson
519 (2005). "Correlative microscopy and electron tomography of GFP through photooxidation." *Nat*
520 *Methods* **2**(11): 857-862.
521 Hariri, M., G. Millane, M. P. Guimond, G. Guay, J. W. Dennis and I. R. Nabi (2000). "Biogenesis
522 of multilamellar bodies via autophagy." *Mol Biol Cell* **11**(1): 255-268.
523 Huh, Y. H., S. J. Bahk, J. Y. Ghee and S. H. Yoo (2005). "Subcellular distribution of
524 chromogranins A and B in bovine adrenal chromaffin cells." *FEBS Lett* **579**(23): 5145-5151.
525 Iancu, C. V., W. F. Tivol, J. B. Schooler, D. P. Dias, G. P. Henderson, G. E. Murphy, E. R. Wright,
526 Z. Li, Z. Yu, A. Briegel, L. Gan, Y. He and G. J. Jensen (2006). "Electron cryotomography sample
527 preparation using the Vitrobot." *Nat Protoc* **1**(6): 2813-2819.
528 Jackson, K. A., D. S. Snyder and M. A. Goodell (2004). "Skeletal muscle fiber-specific green
529 autofluorescence: potential for stem cell engraftment artifacts." *Stem Cells* **22**(2): 180-187.
530 Jun, S., D. Ke, K. Debiec, G. Zhao, X. Meng, Z. Ambrose, G. A. Gibson, S. C. Watkins and P.
531 Zhang (2011). "Direct visualization of HIV-1 with correlative live-cell microscopy and cryo-
532 electron tomography." *Structure* **19**(11): 1573-1581.
533 Kapoor, T. M., M. A. Lampson, P. Hergert, L. Cameron, D. Cimini, E. D. Salmon, B. F. McEwen
534 and A. Khodjakov (2006). "Chromosomes can congress to the metaphase plate before
535 biorientation." *Science* **311**(5759): 388-391.
536 Kelly, R. B. (1985). "Pathways of protein secretion in eukaryotes." *Science* **230**(4721): 25-32.
537 Kim, T., J. H. Tao-Cheng, L. E. Eiden and Y. P. Loh (2001). "Chromogranin A, an "on/off" switch
538 controlling dense-core secretory granule biogenesis." *Cell* **106**(4): 499-509.

- 539 Klionsky, D. J., E. L. Eskelinen and V. Deretic (2014). "Autophagosomes, phagosomes,
540 autolysosomes, phagolysosomes, autophagolysosomes... wait, I'm confused." Autophagy **10**(4):
541 549-551.
- 542 Klumperman, J. and G. Raposo (2014). "The complex ultrastructure of the endolysosomal
543 system." Cold Spring Harb Perspect Biol **6**(10): a016857.
- 544 Konig, K., A. Uchugonova and H. G. Breunig (2014). "High-resolution multiphoton
545 cryomicroscopy." Methods **66**(2): 230-236.
- 546 Kremer, J. R., D. N. Mastronarde and J. R. McIntosh (1996). "Computer visualization of three-
547 dimensional image data using IMOD." J Struct Biol **116**(1): 71-76.
- 548 Kukulski, W., M. Schorb, M. Kaksonen and J. A. Briggs (2012). "Plasma membrane reshaping
549 during endocytosis is revealed by time-resolved electron tomography." Cell **150**(3): 508-520.
- 550 Kukulski, W., M. Schorb, S. Welsch, A. Picco, M. Kaksonen and J. A. Briggs (2011). "Correlated
551 fluorescence and 3D electron microscopy with high sensitivity and spatial precision." J Cell Biol
552 **192**(1): 111-119.
- 553 Kumar, B. S., S. Sandhyamani, S. S. Nazeer and R. S. Jayasree (2015). "Rapid and simple
554 method of photobleaching to reduce background autofluorescence in lung tissue sections." Indian
555 J Biochem Biophys **52**(1): 107-110.
- 556 Lajoie, P., G. Guay, J. W. Dennis and I. R. Nabi (2005). "The lipid composition of autophagic
557 vacuoles regulates expression of multilamellar bodies." J Cell Sci **118**(Pt 9): 1991-2003.
- 558 Lemaire, K., M. A. Ravier, A. Schraenen, J. W. Creemers, R. Van de Plas, M. Granvik, L. Van
559 Lommel, E. Waelkens, F. Chimienti, G. A. Rutter, P. Gilon, P. A. in't Veld and F. C. Schuit (2009).
560 "Insulin crystallization depends on zinc transporter ZnT8 expression, but is not required for
561 normal glucose homeostasis in mice." Proc Natl Acad Sci U S A **106**(35): 14872-14877.
- 562 Liu, B., Y. Xue, W. Zhao, Y. Chen, C. Fan, L. Gu, Y. Zhang, X. Zhang, L. Sun, X. Huang, W.
563 Ding, F. Sun, W. Ji and T. Xu (2015). "Three-dimensional super-resolution protein localization
564 correlated with vitrified cellular context." Sci Rep **5**: 13017.
- 565 Lucic, V., A. Rigort and W. Baumeister (2013). "Cryo-electron tomography: the challenge of doing
566 structural biology in situ." J Cell Biol **202**(3): 407-419.
- 567 Mansfield, J. R., K. W. Gossage, C. C. Hoyt and R. M. Levenson (2005). "Autofluorescence
568 removal, multiplexing, and automated analysis methods for in-vivo fluorescence imaging." J
569 Biomed Opt **10**(4): 41207.
- 570 Marsh, B. J., C. Soden, C. Alarcon, B. L. Wicksteed, K. Yaekura, A. J. Costin, G. P. Morgan and
571 C. J. Rhodes (2007). "Regulated autophagy controls hormone content in secretory-deficient
572 pancreatic endocrine beta-cells." Mol Endocrinol **21**(9): 2255-2269.
- 573 Mastronarde, D. N. (2005). "Automated electron microscope tomography using robust prediction
574 of specimen movements." J Struct Biol **152**(1): 36-51.
- 575 Merglen, A., S. Theander, B. Rubi, G. Chaffard, C. B. Wollheim and P. Maechler (2004).
576 "Glucose sensitivity and metabolism-secretion coupling studied during two-year continuous
577 culture in INS-1E insulinoma cells." Endocrinology **145**(2): 667-678.
- 578 Muller-Reichert, T., M. Srayko, A. Hyman, E. T. O'Toole and K. McDonald (2007). "Correlative
579 light and electron microscopy of early *Caenorhabditis elegans* embryos in mitosis." Methods Cell
580 Biol **79**: 101-119.
- 581 Neumann, M. and D. Gabel (2002). "Simple method for reduction of autofluorescence in
582 fluorescence microscopy." J Histochem Cytochem **50**(3): 437-439.
- 583 Nickell, S., C. Kofler, A. P. Leis and W. Baumeister (2006). "A visual approach to proteomics."
584 Nat Rev Mol Cell Biol **7**(3): 225-230.

585 Oikonomou, C. M. and G. J. Jensen (2016). "A new view into prokaryotic cell biology from
586 electron cryotomography." Nat Rev Microbiol **14**(4): 205-220.

587 Orci, L., M. Ravazzola, M. Amherdt, O. Madsen, A. Perrelet, J. D. Vassalli and R. G. Anderson
588 (1986). "Conversion of proinsulin to insulin occurs coordinately with acidification of maturing
589 secretory vesicles." J Cell Biol **103**(6 Pt 1): 2273-2281.

590 Paroutis, P., N. Touret and S. Grinstein (2004). "The pH of the secretory pathway: measurement,
591 determinants, and regulation." Physiology (Bethesda) **19**: 207-215.

592 Rabl, R., V. Soubannier, R. Scholz, F. Vogel, N. Mendl, A. Vasiljev-Neumeyer, C. Korner, R.
593 Jagasia, T. Keil, W. Baumeister, M. Cyrklaff, W. Neupert and A. S. Reichert (2009). "Formation of
594 cristae and crista junctions in mitochondria depends on antagonism between Fcj1 and Su e/g." J
595 Cell Biol **185**(6): 1047-1063.

596 Redemann, S. and T. Muller-Reichert (2013). "Correlative light and electron microscopy for the
597 analysis of cell division." J Microsc **251**(2): 109-112.

598 Rubi, B., S. Ljubicic, S. Pournourmohammadi, S. Carobbio, M. Armanet, C. Bartley and P.
599 Maechler (2005). "Dopamine D2-like receptors are expressed in pancreatic beta cells and
600 mediate inhibition of insulin secretion." J Biol Chem **280**(44): 36824-36832.

601 Schellenberger, P., R. Kaufmann, C. A. Siebert, C. Hagen, H. Wodrich and K. Grunewald (2014).
602 "High-precision correlative fluorescence and electron cryo microscopy using two independent
603 alignment markers." Ultramicroscopy **143**: 41-51.

604 Schlimpert, S., E. A. Klein, A. Briegel, V. Hughes, J. Kahnt, K. Bolte, U. G. Maier, Y. V. Brun, G.
605 J. Jensen, Z. Gitai and M. Thanbichler (2012). "General protein diffusion barriers create
606 compartments within bacterial cells." Cell **151**(6): 1270-1282.

607 Schnell, S. A., W. A. Staines and M. W. Wessendorf (1999). "Reduction of lipofuscin-like
608 autofluorescence in fluorescently labeled tissue." J Histochem Cytochem **47**(6): 719-730.

609 Schorb, M. and J. A. Briggs (2014). "Correlated cryo-fluorescence and cryo-electron microscopy
610 with high spatial precision and improved sensitivity." Ultramicroscopy **143**: 24-32.

611 Schorb, M., L. Gaechter, O. Avinoam, F. Sieckmann, M. Clarke, C. Bebeacua, Y. S. Bykov, A. F.
612 Sonnen, R. Lihl and J. A. Briggs (2016). "New hardware and workflows for semi-automated
613 correlative cryo-fluorescence and cryo-electron microscopy/tomography." J Struct Biol.

614 Schwartz, C. L., V. I. Sarbash, F. I. Ataullakhanov, J. R. McIntosh and D. Nicastro (2007). "Cryo-
615 fluorescence microscopy facilitates correlations between light and cryo-electron microscopy and
616 reduces the rate of photobleaching." J Microsc **227**(Pt 2): 98-109.

617 Sheen, J., S. Hwang, Y. Niwa, H. Kobayashi and D. W. Galbraith (1995). "Green-fluorescent
618 protein as a new vital marker in plant cells." Plant J **8**(5): 777-784.

619 Steinkamp, J. A. and C. C. Stewart (1986). "Dual-laser, differential fluorescence correction
620 method for reducing cellular background autofluorescence." Cytometry **7**(6): 566-574.

621 Szollosi, J., S. J. Lockett, M. Balazs and F. M. Waldman (1995). "Autofluorescence correction for
622 fluorescence in situ hybridization." Cytometry **20**(4): 356-361.

623 Taupenot, L., K. L. Harper and D. T. O'Connor (2003). "The chromogranin-secretogranin family."
624 N Engl J Med **348**(12): 1134-1149.

625 Taupenot, L., K. L. Harper and D. T. O'Connor (2005). "Role of H⁺-ATPase-mediated
626 acidification in sorting and release of the regulated secretory protein chromogranin A: evidence
627 for a vesiculogenic function." J Biol Chem **280**(5): 3885-3897.

628 Van de Lest, C. H., E. M. Versteeg, J. H. Veerkamp and T. H. Van Kuppevelt (1995). "Elimination
629 of autofluorescence in immunofluorescence microscopy with digital image processing." J
630 Histochem Cytochem **43**(7): 727-730.

631 Videen, J. S., M. S. Mezger, Y. M. Chang and D. T. O'Connor (1992). "Calcium and
632 catecholamine interactions with adrenal chromogranins. Comparison of driving forces in binding
633 and aggregation." J Biol Chem **267**(5): 3066-3073.

634 Viegas, M. S., T. C. Martins, F. Seco and A. do Carmo (2007). "An improved and cost-effective
635 methodology for the reduction of autofluorescence in direct immunofluorescence studies on
636 formalin-fixed paraffin-embedded tissues." Eur J Histochem **51**(1): 59-66.

637 Voloshin Ia, M., I. Suslov Ie, P. I. Chepel, V. F. Kovalenchenko and V. V. Polishchuk (2000).
638 "[The pulmonary microangiopathy in patients with tuberculosis coexisting with diabetes mellitus]."
639 Klin Khir(11): 37-39.

640 Yoo, S. H. and J. P. Albanesi (1991). "High capacity, low affinity Ca²⁺ binding of chromogranin
641 A. Relationship between the pH-induced conformational change and Ca²⁺ binding property." J
642 Biol Chem **266**(12): 7740-7745.

643 Zheng, S. Q., B. Keszthelyi, E. Branlund, J. M. Lyle, M. B. Braunfeld, J. W. Sedat and D. A.
644 Agard (2007). "UCSF tomography: an integrated software suite for real-time electron microscopic
645 tomographic data collection, alignment, and reconstruction." J Struct Biol **157**(1): 138-147.

646 Zick, M., R. Rabl and A. S. Reichert (2009). "Cristae formation-linking ultrastructure and function
647 of mitochondria." Biochim Biophys Acta **1793**(1): 5-19.

648

649

650

651

652

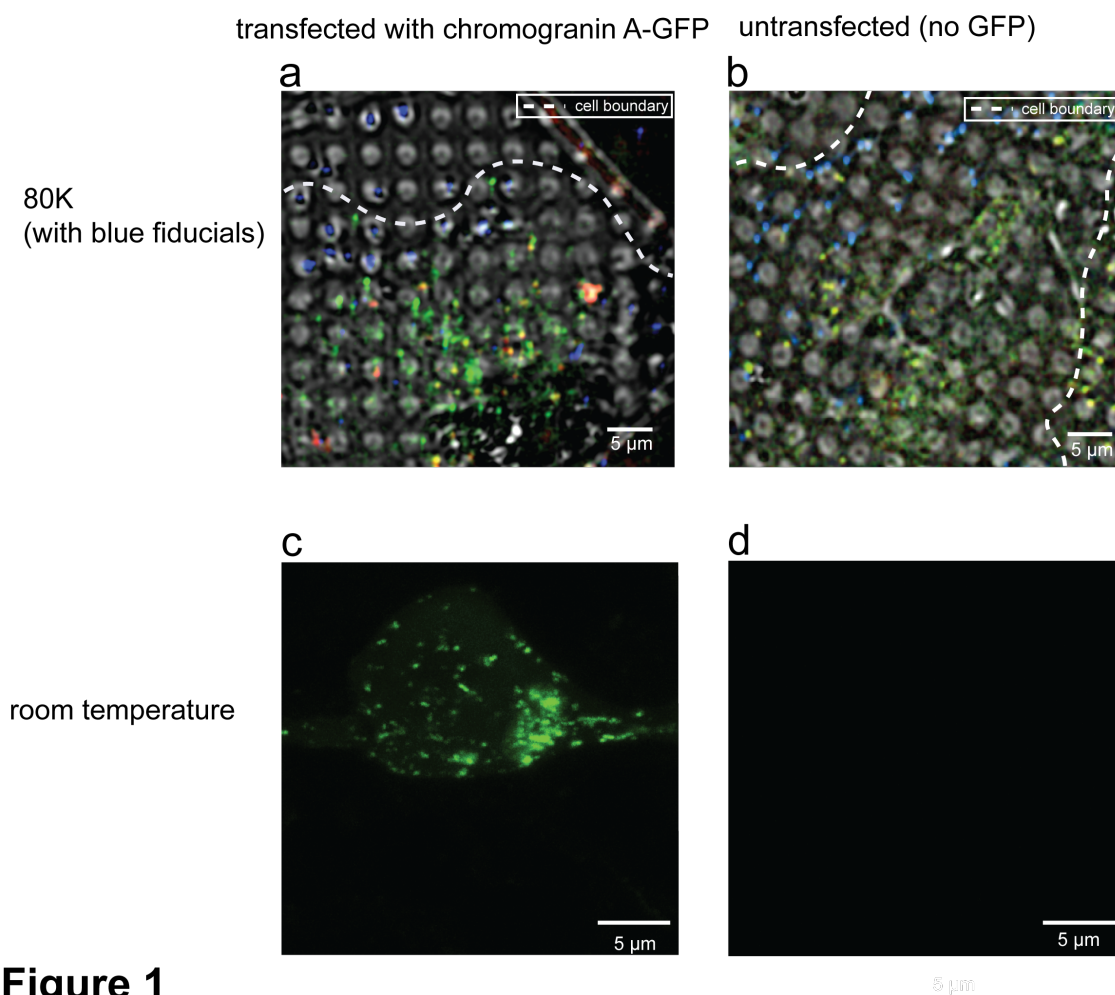


Figure 1

653

654

655

656

657

658

659

660

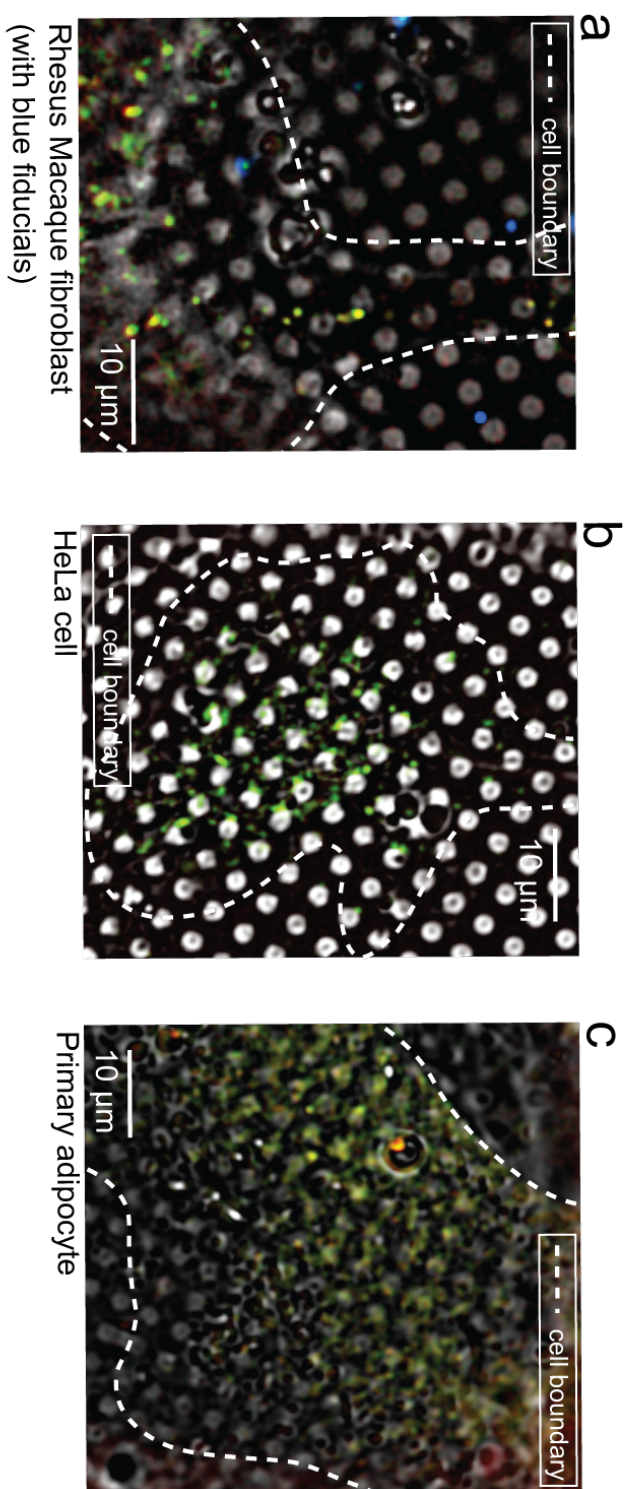
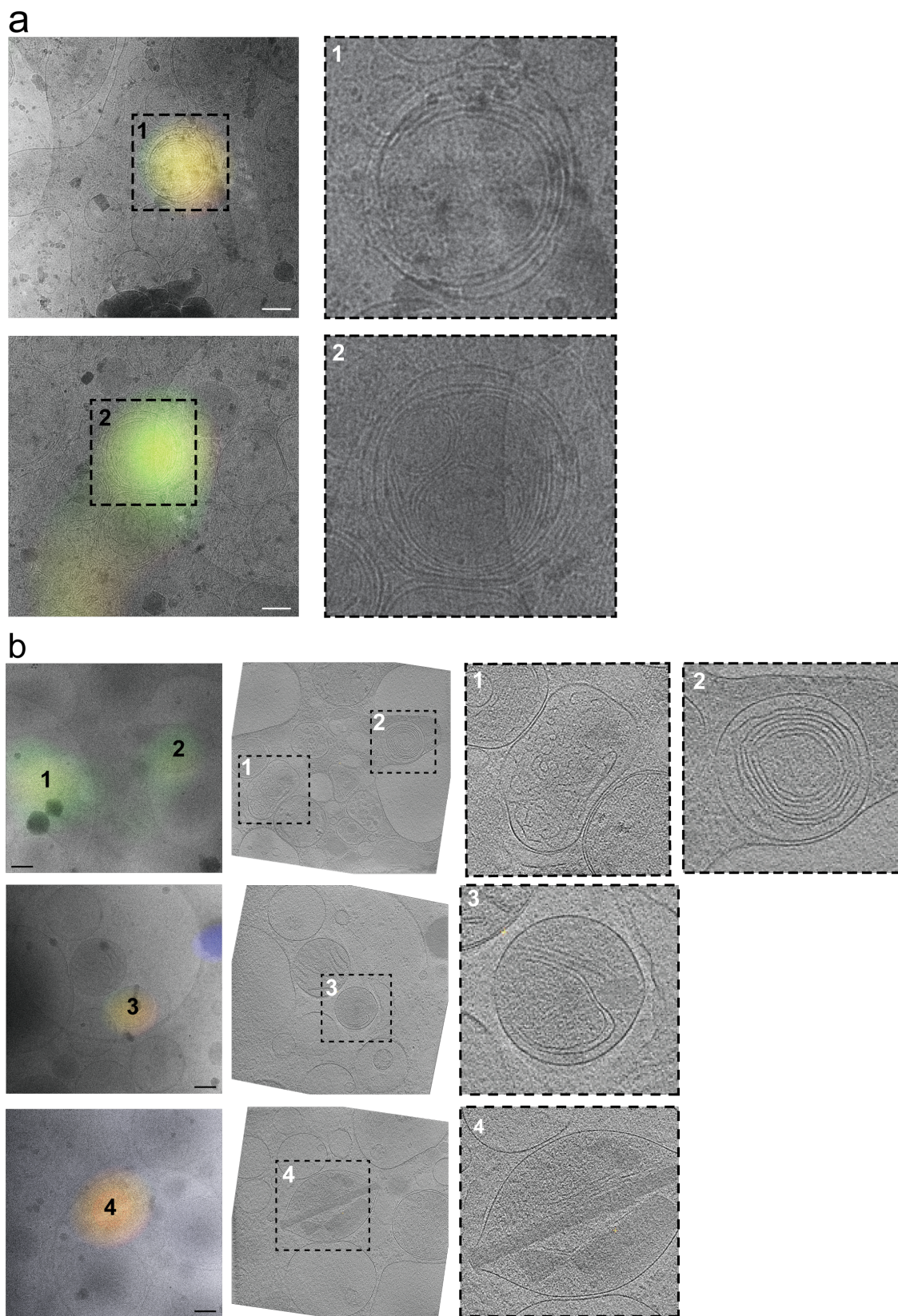
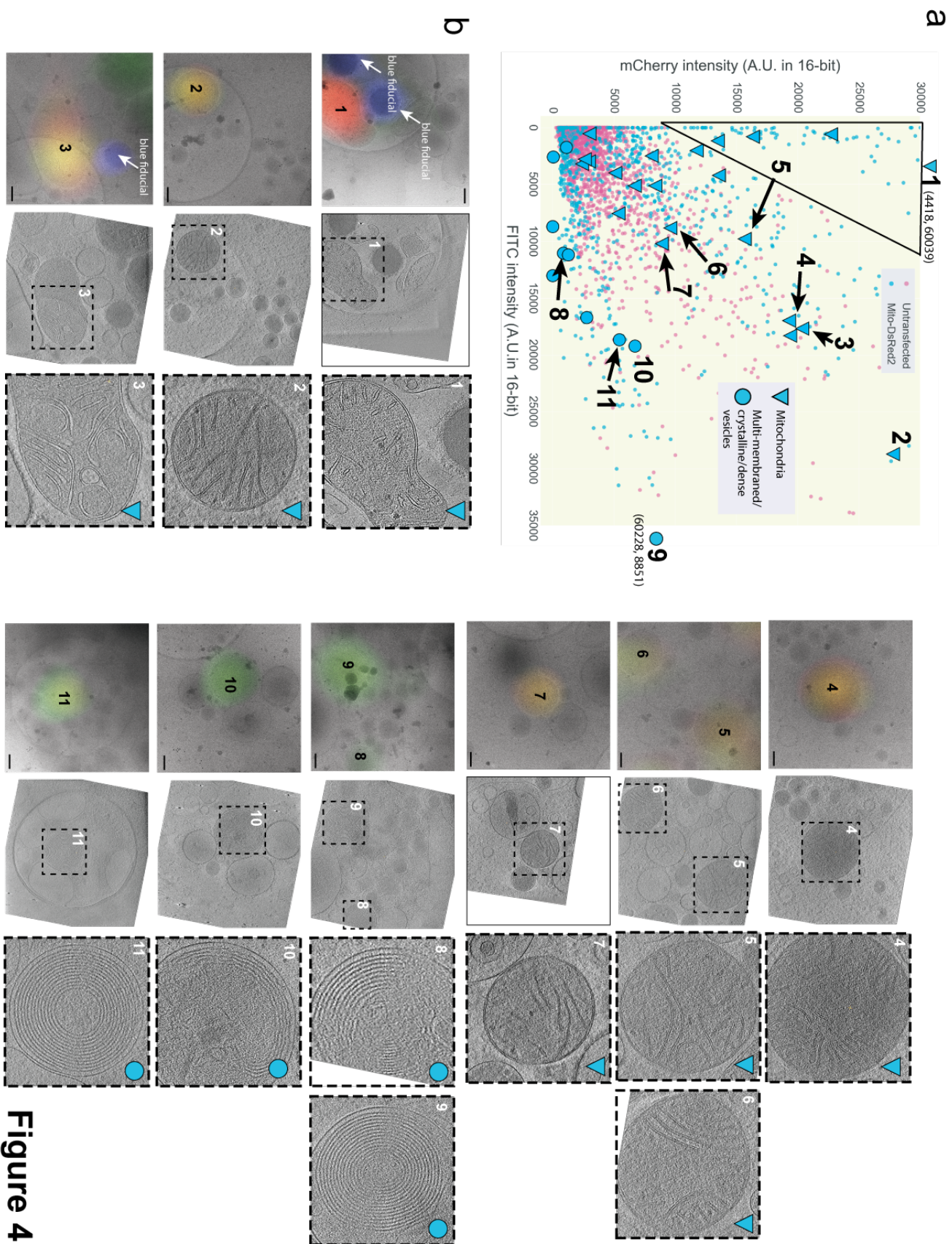


Figure 2





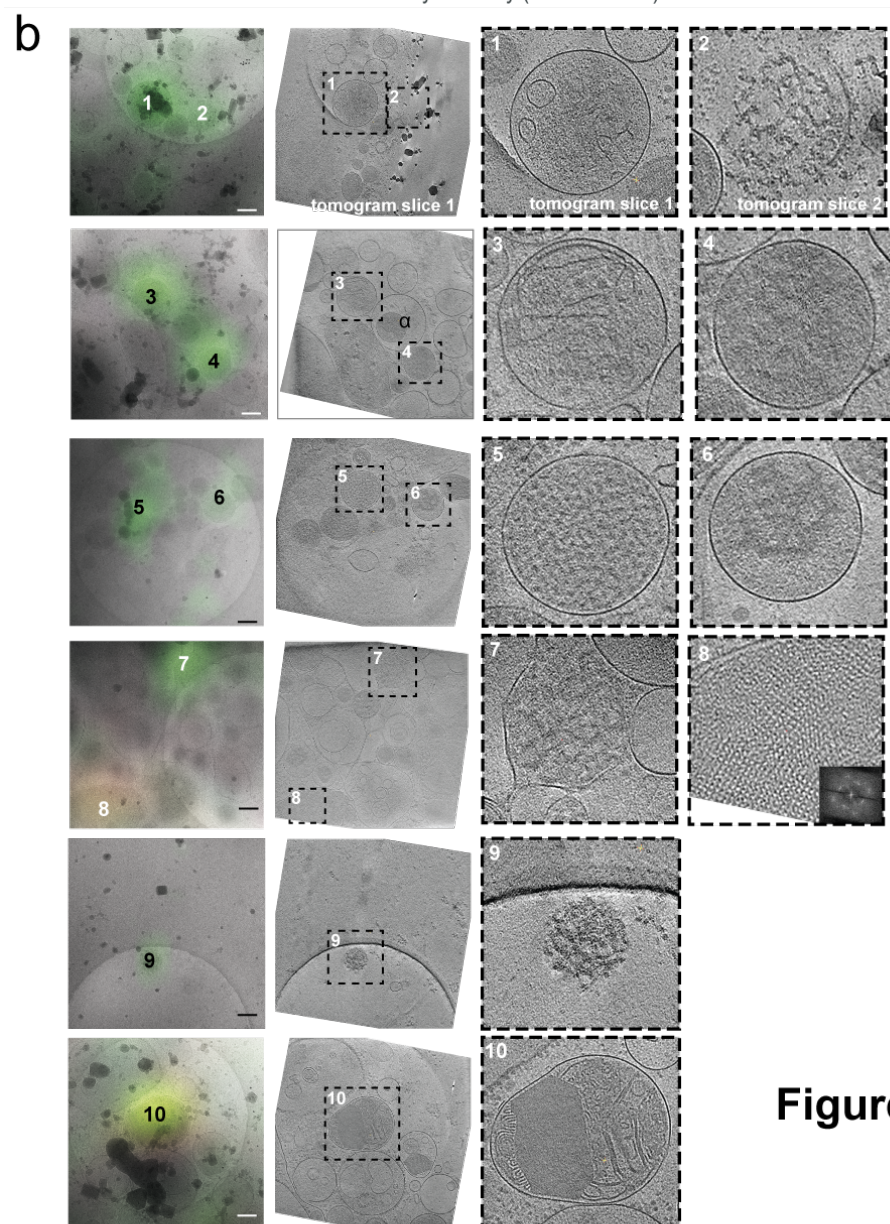
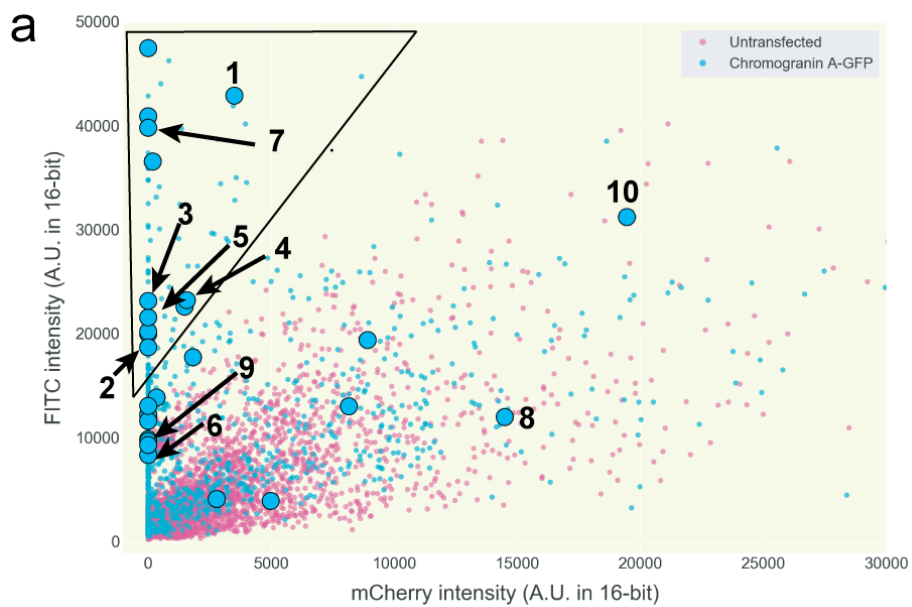


Figure 5